

In Situ Phase-Transition Crystallization of All-Inorganic Water-Resistant Exciton-Radiative Heteroepitaxial CsPbBr₃–CsPb₂Br₅ Core–Shell Perovskite Nanocrystals

Tianyuan Liang, Wenjie Liu, Xiaoyu Liu, Yuanyuan Li, Wenhui Wu, and Jiyang Fan*

School of Physics, Southeast University, Nanjing 211189, P. R. China

Corresponding Author

*E-mail: jyfan@seu.edu.cn

ABSTRACT: The instability of metal halide perovskites upon exposure to moisture or heat strongly hampers their applications in optoelectronic devices. Here, we report the large-yield synthesis of highly water-resistant total-inorganic green luminescent CsPbBr₃/CsPb₂Br₅ core/shell heteronanocrystals (HNCs) by developing an in situ phase transition approach. It is implemented via water-driven phase transition of the original monoclinic CsPbBr₃ nanocrystal and the resultant tetragonal CsPb₂Br₅ nanoshell has small lattice mismatch with the CsPbBr₃ core, which ensures formation of an epitaxial interface for the yielded CsPbBr₃/CsPb₂Br₅ HNC. These HNCs maintain nearly 100% of the original luminescence intensity after immersion in water for eleven months and the luminescence intensity drops only to 81.3% at 100 °C. The transient luminescence spectroscopy and density functional theory calculation reveal that there are double

radiative recombination channels in the core CsPbBr₃ nanocrystal, and the electron potential barrier provided by the CsPb₂Br₅ nanoshell significantly improves the exciton recombination rate. A prototype quasi-white light-emitting device based on these robust CsPbBr₃/CsPb₂Br₅ HNCs is realized, showing their strong competence in solid-state lighting and wide color-gamut displays.

1. INTRODUCTION

In the past few years, the metal halide perovskites have attracted great interest due to their very wide crystal structure spectrum and excellent electrical and optical properties.^{1,2} For example, the power conversion efficiency of the perovskite solar cells has reached up to 25% and is comparable to that of the conventional silicon solar cells.³ Although there could be the quantum efficiency droop (gradual drop) problem,⁴ the investigators have tried to fabricate perovskite light-emitting devices with external quantum efficiencies > 20%.⁵⁻⁷ Some novel types of perovskites such as layered perovskites⁸ and zero-dimensional perovskites⁹ show broadband white luminescence¹⁰ or near-UV luminescence [such as self-trapped exciton quantum confinement luminescence of Cs₄PbCl₆ or Cs₄PbBr₆^{11,12}], and they bring more hopes for realization of perovskite-based optoelectronic devices. Although perovskites have many virtues, but their instability upon exposure to moisture or heat strongly hampers their practical applications.¹³⁻¹⁵ This is particularly serious for the self-assembly crystallized organic-inorganic hybrid perovskites¹⁶ and limits their device applications.¹⁷⁻¹⁹ Another large family of perovskites are the all-inorganic CsPbX₃ (X = Cl, Br, and I)²⁰ and their nanocrystals (NCs) have aroused high interest owing to better stability and good luminescence properties.²¹⁻²⁴ However, even the CsPbX₃ NCs have poor stability upon exposure to humidity, light, or heat.²⁵⁻²⁸ The studies of the conventional core/shell semiconductor heterostructures reveal that the existence of a shell can

significantly influence the migration of the photogenerated carriers in the core and control the luminescence properties.²⁹⁻³⁴ The shell also improves stability of the core nanocrystal.^{35,36} Therefore, some researchers have conceived to synthesize core-shell nanostructures to improve stability of the perovskite NCs.³⁷⁻³⁹ However, because the perovskites have fragile ionic structures, the previous study has been limited to synthesis of the core-shell perovskite nanostructures employing various kinds of amorphous oxides (SiO₂, TiO₂, and ZrO₂) as the encapsulation layers.⁴⁰⁻⁴³ There have also been reports on synthesis of the composite materials composed of perovskites and chalcogenides (CdS, ZnS, PbS, and PbSe).⁴⁴⁻⁴⁷ For most of these materials, it is unclear whether the perovskite is epitaxially fused with another material.³⁷

The previous study revealed that the synthesized millimeter-sized CsPbBr₃ crystals contained a small amount of CsPb₂Br₅ (10%) as the byproduct.⁴⁸ In fact, the ternary phase diagram of Cs, Pb, and Br (Figure 1b) indicates that monoclinic CsPbBr₃, tetragonal CsPb₂Br₅ (Figure 1c), and hexagonal Cs₄PbBr₆ lie on the same segment whose endpoints are PbBr₂ and CsBr. This explains why CsPbBr₃ and CsPb₂Br₅ often coexist in the product, although they are only a mixture⁴⁹⁻⁵¹ rather than heteronanocrystals (HNCs). There have been reports on synthesis of dual-phase CsPbBr₃-CsPb₂Br₅ perovskite films and dual-phase halide perovskite nanorings, which are not core-shell structures.^{52,53} On the other hand, it has been known that CsPbBr₃ may decompose into CsPb₂Br₅ in water following $2\text{CsPbBr}_3 \xrightarrow{\text{H}_2\text{O}} \text{CsBr} + \text{CsPb}_2\text{Br}_5$.⁵⁴ Herein, we develop an in situ phase transition strategy to synthesize highly water-resistant luminescent CsPbBr₃/CsPb₂Br₅ core/shell HNCs. They have good epitaxial crystallization at the core-shell interface. Both their microstructures and luminescence properties exhibit high water and thermal stability. The implementation of a prototype white light-emitting diode (LED) based on these HNCs demonstrates their strong application potential in lighting and displays.

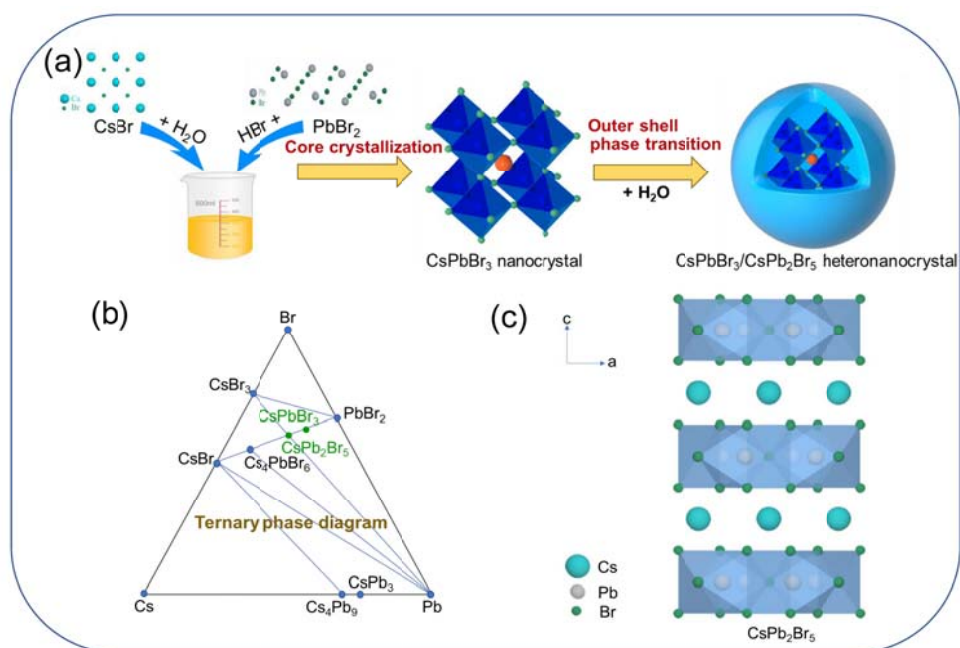


Figure 1. (a) Schematic diagram showing synthesis strategy of the CsPbBr₃/CsPb₂Br₅ core/shell HNC. (b) Ternary phase diagram of Cs, Pb, and Br. CsPbBr₃ and CsPb₂Br₅ lie between the precursors CsBr and PbBr₂ on the segment. (c) Crystal structure of tetragonal CsPb₂Br₅.

2. RESULTS AND DISCUSSION

2.1. Microstructure of Phase Transition Induced Heteronanocrystals. Figure 1a shows the synthesis strategy of the CsPbBr₃/CsPb₂Br₅ core/shell HNCs. In brief, PbBr₂ in hydrobromic acid and CsBr in deionized water reacted to yield an orange powder containing CsPbBr₃ NCs. It should be noted that the CsPbBr₃ NCs (orange powder) were synthesized in the hydrobromic acid solution and only a small amount of deionized water [CsBr (10 mmol) in water (3 mL) mixed with PbBr₂ (10 mmol) in HBr (8 mL)] was used to dissolve CsBr. When the synthesized

CsPbBr₃ orange powder was immersed in a large amount of deionized water and stirred, the surfaces of the CsPbBr₃ NCs lost CsBr owing to the action of water, leading to their in situ phase transition to become CsPb₂Br₅. The generated CsPb₂Br₅ on the surfaces of the CsPbBr₃ NCs prevented water from further penetrating into the interior of the CsPbBr₃ NCs and thus the CsPbBr₃/CsPb₂Br₅ core/shell HNCs (white powder) formed. The orange powder exhibited no naked-eye-identifiable photoluminescence (PL) under UV-light excitation (inset of Figure 2a). Figure 2a shows its X-ray diffraction (XRD) pattern, and most of the diffraction peaks can be identified as those of monoclinic CsPbBr₃ (PDF#18-0364), but some weaker peaks are identified as those of tetragonal CsPb₂Br₅ (PDF#25-0211). This agrees with the previous finding that the synthesized CsPbBr₃ crystallites often contain a small amount of CsPb₂Br₅.⁴⁸ The detailed comparison (Figure S1) confirms that the orange powder is indeed monoclinic CsPbBr₃ rather than the other structured CsPbBr₃. Unlike monoclinic CsPbBr₃ that is composed of interconnected [PbBr₆]⁴⁻ octahedra (Figure 2c), tetragonal CsPb₂Br₅ is composed of quasi-two dimensional periodic [Pb₂Br₅]⁻ layers that are separated by the intermediate Cs⁺ layers (Figures 1c and 2c). The white powder exhibits very bright green luminescence under UV-light excitation (inset of Figure 2b). Its XRD pattern (Figure 2b) contains mainly diffraction signals of tetragonal CsPb₂Br₅, but it also contains some weak diffraction peaks belonging to monoclinic CsPbBr₃. Since CsPbBr₃ decomposes readily in water, so it is strange why the white powder transformed from the original orange powder in water contains CsPbBr₃. The transmission electron microscopy (TEM) reveals the reason. The high-resolution TEM (HRTEM) image of the orange powder (Figure S2a) reveals that the orange powder contains agglomerates composed of closely and tightly bound nanoparticles with sizes of 10–36 nm (Figure S3). These nanoparticles have good crystallinity (Figure S2b–d), and the measured lattice spacing values are 4.13 and 2.92/2.91

Å, being consistent with that of the (110) and $(\bar{2}00)$ planes of monoclinic CsPbBr₃. Figure S2e shows the corresponding selected-area electron diffraction (SAED) pattern, and the bright

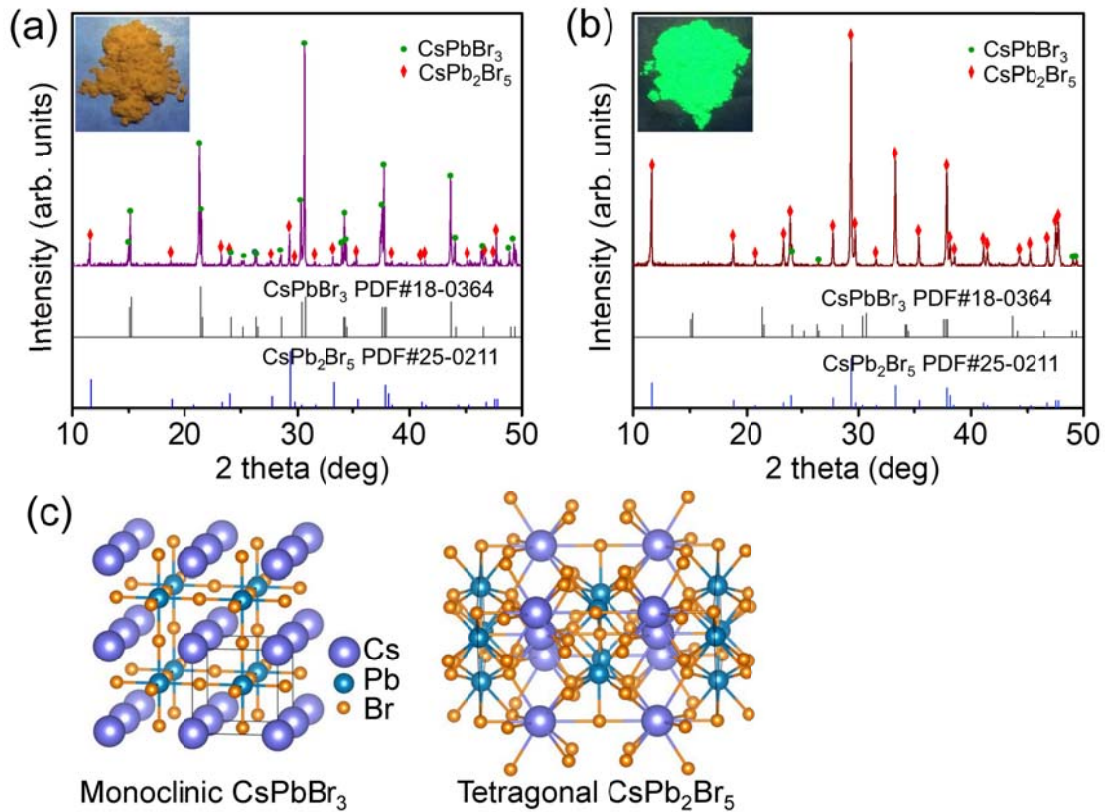


Figure 2. XRD patterns of (a) orange powder and (b) white powder. Blue bars show standard XRD patterns of monoclinic CsPbBr₃ and tetragonal CsPb₂Br₅. Inset shows luminescence photos under 365-nm excitation. (c) Crystal structures of monoclinic CsPbBr₃ and tetragonal CsPb₂Br₅.

diffraction spots are separately ascribed to the (110), $(\bar{2}00)$, and $(\bar{2}20)$ planes of monoclinic CsPbBr₃. The CsPb₂Br₅ nanoparticles are not identified from the HRTEM images, suggesting their quantity should be small and thus can only be identified from the XRD pattern.

The HRTEM image of the white powder (Figure 3a) reveals that it is composed of individual core/shell NCs with sizes of 15–33 nm and core sizes of 4–14 nm (Figure S4). The ratios of the diameters of the cores and core/shell structures range from 0.2 to 0.5. The contrast of the core and shell exhibited in the TEM image is remarkable, suggesting their different compositions. Figure 3b shows the fast Fourier transform (FFT) of the HRTEM image in Figure 3a, and bright spots correspond to the (310) planes of CsPb_2Br_5 and $(\bar{2}00)$ and $(\bar{1}11)$ planes of CsPbBr_3 , respectively (Figure 3c). Figure 3d shows a magnified HRTEM image of a typical core/shell nanoparticle. The lattice spacing of the core is 2.90 Å, being consistent with that of the $(\bar{2}00)$ planes of monoclinic CsPbBr_3 , and the lattice spacing of the shell is 4.23 Å, corresponding to the (200) planes of tetragonal CsPb_2Br_5 . Figure 3e shows the FFT of Figure 3d. It comprises bright spots belonging to the (200) planes of CsPb_2Br_5 and $(\bar{2}00)$ planes of CsPbBr_3 (Figure 3f), and the angle between these planes is derived to be 45°. Figure 3g shows the corresponding lattice matching relation of the CsPbBr_3 – CsPb_2Br_5 interface and Figure 3h,i show the lattice models of tetragonal CsPb_2Br_5 and monoclinic CsPbBr_3 . The interface is composed of the parallel CsPb_2Br_5 :(200) plane and CsPbBr_3 :(110). The separation angle between the CsPb_2Br_5 :(200) plane and CsPbBr_3 :($\bar{2}00$) plane is 45°. The CsPb_2Br_5 :(002) planes and CsPbBr_3 :($\bar{1}10$) planes are perpendicular to the interface. We have $d(002) = 7.63 \text{ \AA}$, $2 \times d(\bar{1}10) = 8.20 \text{ \AA}$, so the lattice mismatch between them is 7.2%; the lattice mismatch between the CsPb_2Br_5 :(200) plane ($d = 4.25 \text{ \AA}$) and CsPbBr_3 :(110) plane ($d = 4.13 \text{ \AA}$) is 2.9%. In addition, Figure 3d,f also shows the lattice fringe and diffraction spots belonging to (004) lattice planes ($d = 3.80 \text{ \AA}$) of CsPb_2Br_5 . As shown in the lattice model of Figure 3h,i, the CsPb_2Br_5 :(004) planes ($d = 3.81 \text{ \AA}$) and CsPbBr_3 :($\bar{1}10$) planes ($d = 4.10 \text{ \AA}$) are parallel to each other, and they constitute the upper interface shown in Figure 3d, with a lattice mismatch of 7.3%. The CsPb_2Br_5 :(300) planes and

CsPbBr₃:(110) planes are perpendicular to this interface. We have $3 \times d(300) = 8.49 \text{ \AA}$, $2 \times d(110) = 8.26 \text{ \AA}$, so the lattice mismatch between them is 2.7%. Therefore, the lattice mismatch along

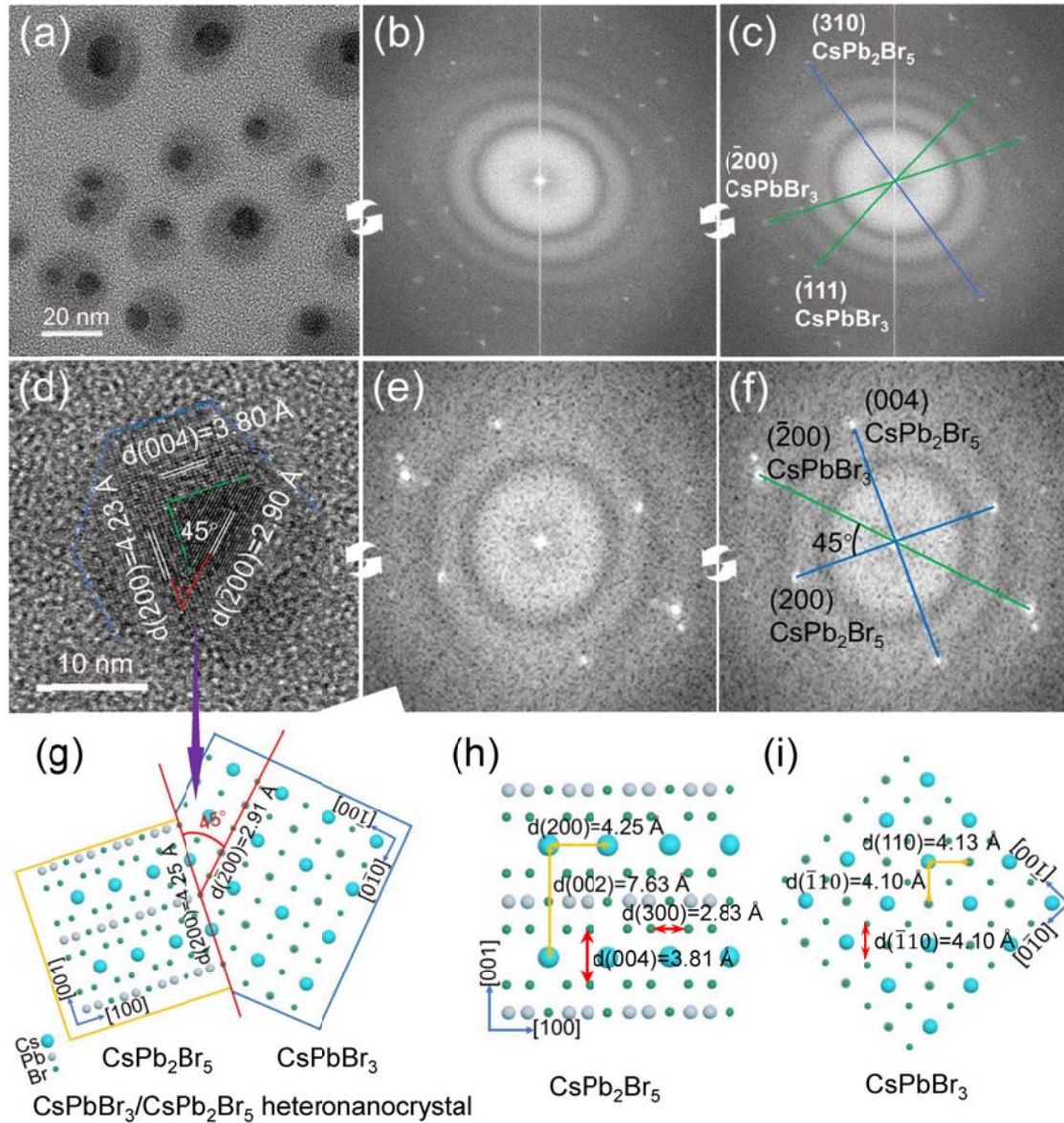


Figure 3. (a) HRTEM image of the CsPbBr₃/CsPb₂Br₅ core/shell HNCs in the white powder. (b, c) FFT of the image in (a). (d) HRTEM image of a typical HNC and (e, f) corresponding FFT.

Green and blue lines in (d) indicate core and shell regions, respectively. (g) Lattice matching relation at the interface of the CsPbBr₃/CsPb₂Br₅ core/shell HNC corresponding to that shown in (d). Crystal structures of (h) CsPb₂Br₅ and (i) CsPbBr₃ with marked lattice spacing values.

the direction either parallel or perpendicular to the interface is small, which ensures epitaxial crystallization of CsPb₂Br₅ and CsPbBr₃ at the interface of the HNC. The HRTEM observation reveals there is another type of epitaxial crystallization of the CsPb₂Br₅–CsPbBr₃ interface in the core/shell HNC, as shown in Figure 4. The FFT (Figure 4b,c) of the core/shell HNC shown in Figure 4a contains the bright spots belonging to the (200) and (220) planes of tetragonal CsPb₂Br₅, and the angle between them is measured to be 45°. There are some additional spots in the FFT image that belong to the ($\bar{2}01$) planes of CsPbBr₃. The magnified HRTEM image (Figure 4e) exhibits remarkable Moiré fringe in the core area, and it arises from the spatial overlap of the lattice planes of the CsPbBr₃ core and that of the CsPb₂Br₅ shell. The existence of the Moiré pattern demonstrates that the lattice planes of the core and those of the shell at the interface are nearly parallel and thus reveals the heteroepitaxial nature of the core–shell interface. The measurement of the lattice spacings indicates that the nearly parallel overlapped lattice planes are the (220) planes of CsPb₂Br₅ ($d = 3.01 \text{ \AA}$) and ($\bar{2}01$) planes of CsPbBr₃ (2.61 \AA). This is consistent with the orientation relation of the corresponding FFT spots (Figure 4c). The lattice mismatch between these two groups of lattice planes is 13%, suggesting there can be strain at the interface. The separation angle between the CsPb₂Br₅:(220) planes and CsPbBr₃:($\bar{2}01$) planes is measured to be 8°, which agrees with the separation angle between the corresponding FFT spots (Figure 4c). The spacing of the Moiré fringe obeys $D = d_1 d_2 / \sqrt{(d_1 - d_2)^2 + d_1 d_2 \alpha^2}$, where d_1 and d_2 are the spacings of the nearly parallel and overlapped lattice planes of the core and shell,

and α is the separation angle between them. We have $d_1 = 3.01 \text{ \AA}$ [CsPb_2Br_5 :(220) plane], $d_2 = 2.61 \text{ \AA}$ [CsPbBr_3 :($\bar{2}01$) plane], and $\alpha = 8^\circ$, so D is calculated to be 1.4 nm, which is consistent with the measured value of 1.45 nm (Figure 4e). The HRTEM observation reveals that the CsPbBr_3 core and CsPb_2Br_5 shell have different ways of lattice matching at their epitaxial interface.

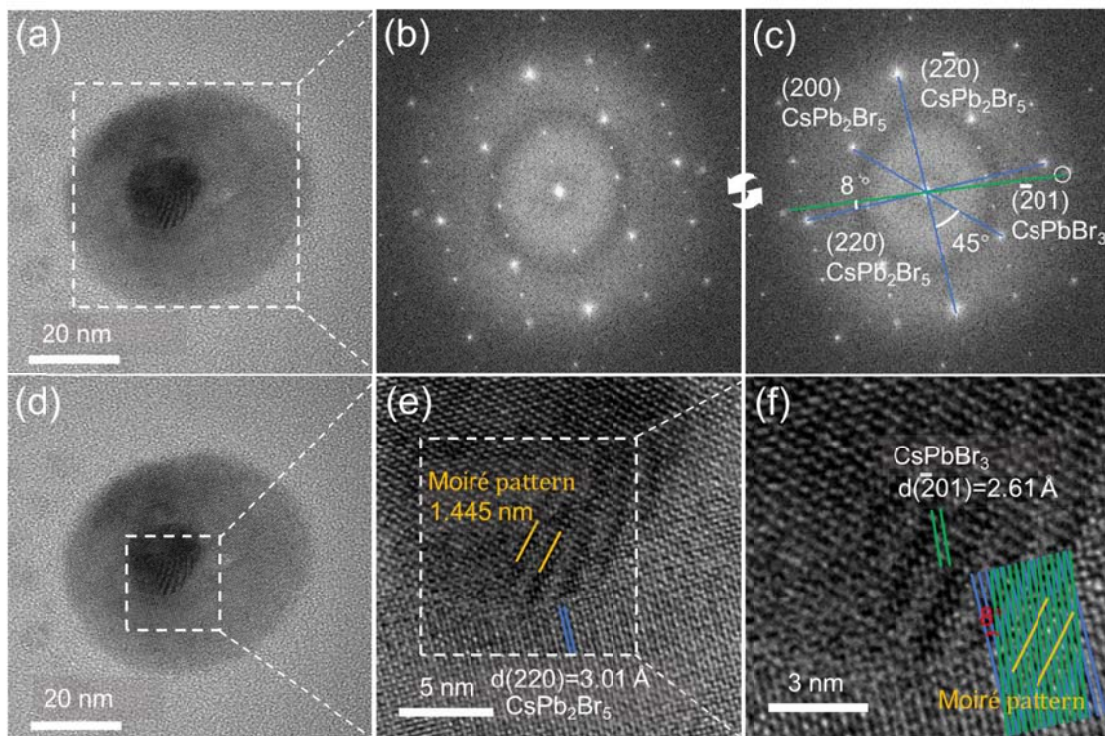


Figure 4. (a, d) HRTEM image of a typical $\text{CsPbBr}_3/\text{CsPb}_2\text{Br}_5$ core/shell HNC in the white powder. (b, c) Corresponding FFT. (e, f) Enlarged image of the marked area in (d).

2.2. Optical Properties and Electronic Structures of $\text{CsPbBr}_3/\text{CsPb}_2\text{Br}_5$ HNCs. The orange powder exhibited rather weak luminescence in that it contains micrometer-sized

composites composed of agglomerated CsPbBr₃ NCs. In contrast, the white powder composed of CsPbBr₃/CsPb₂Br₅ core/shell HNCs emits bright green light. As shown in Figure S5a, the PL peak of the CsPbBr₃ NCs lies at 525 nm, which is consistent with the corresponding exciton absorption peak, indicating the exciton emission nature. The PL peak of the CsPbBr₃/CsPb₂Br₅

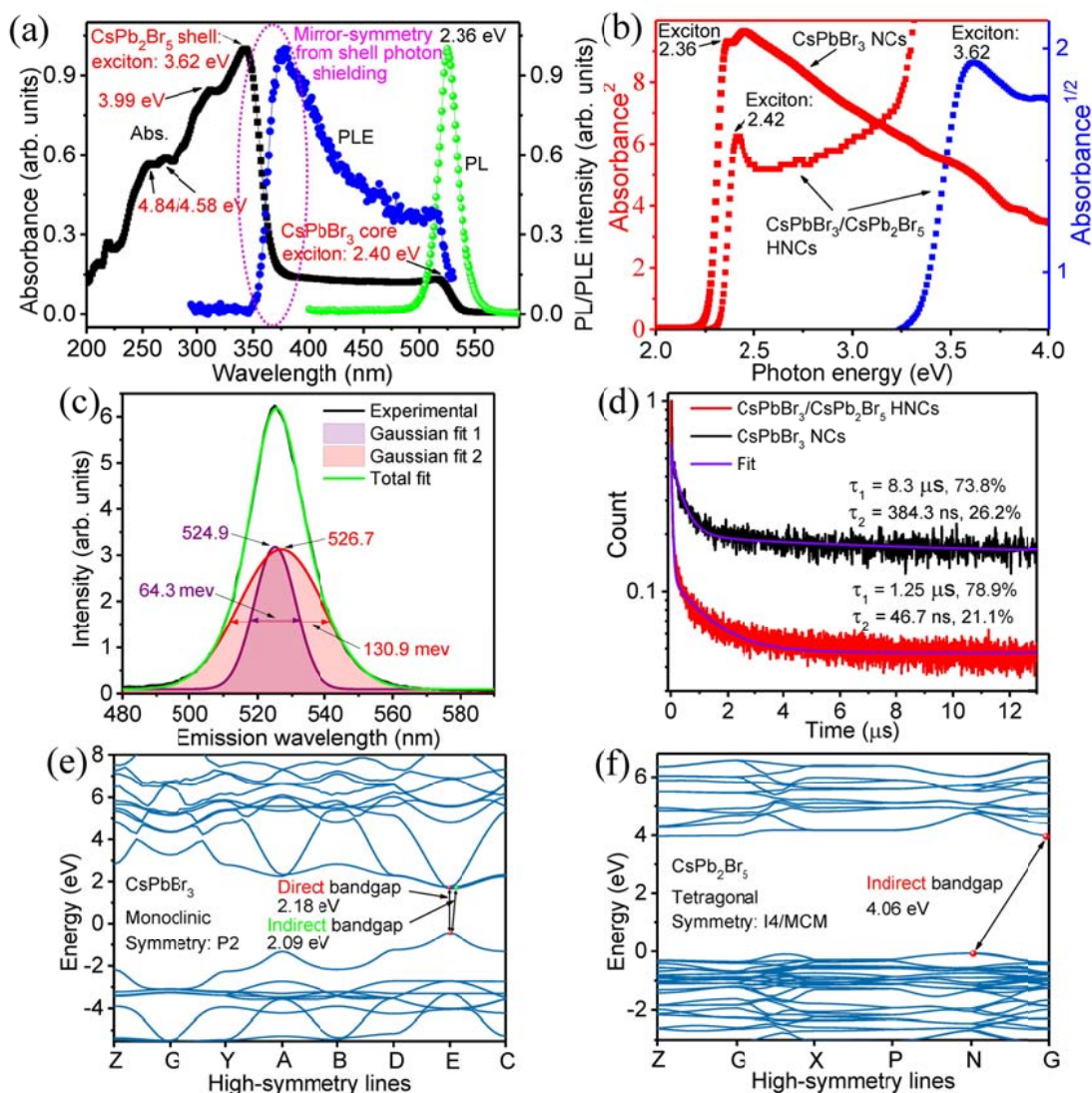


Figure 5. (a) UV–Vis absorption, PL (excitation: 380 nm), and PL excitation (emission: 550 nm) spectra of the CsPbBr₃/CsPb₂Br₅ core/shell HNC white powder. (b) Square and square root of

absorbance versus photon energy for the CsPbBr₃/CsPb₂Br₅ HNCs and squared absorbance vs. photon energy for CsPbBr₃ NCs in the orange powder. (c) Double-Gaussian fit of the PL spectrum of the CsPbBr₃/CsPb₂Br₅ HNCs (excitation: 380 nm). (d) Time-resolved PL spectra and biexponential fits for the CsPbBr₃ NCs and CsPbBr₃/CsPb₂Br₅ HNCs (excitation: 370 nm; emission: 520 nm), respectively. Calculated electronic structure of (e) monoclinic CsPbBr₃ and (f) tetragonal CsPb₂Br₅ by using the DFT method employing the HSE06 exchange–correlation functional.

core/shell HNCs and that of the CsPbBr₃ NCs (Figure S5b) are very close, and this suggests that they have the same origin of luminescence, that is, arising from CsPbBr₃. It should be noted that the shell growth reduces the number of surface dangling bonds with potential trap states for the carriers and thereby improves the fluorescence intensity; however, it does not necessarily cause blue shift of the luminescence.⁵⁵ Figure 5a shows the PL, PL excitation (PLE), and UV–Vis absorption spectra of the white powder containing the CsPbBr₃/CsPb₂Br₅ HNCs. The PL spectrum is narrow, being characteristic of the exciton luminescence of the metal halide perovskites. Its maximum lies at 525 nm (2.36 eV). The PL peak remains nearly fixed when the excitation photon energy is changed (Figure S6) and this suggests there is only weak quantum confinement effect⁵⁶ in that the sizes of the core CsPbBr₃ NCs are bigger than the exciton Bohr diameter. The quantum yield of the CsPbBr₃/CsPb₂Br₅ HNCs was measured to be 13.0% under 374 nm excitation. In contrast, the quantum yield of the CsPbBr₃ NCs was as small as 0.07% (this value is not accurate enough because of the very weak luminescence signal). The UV–Vis absorption spectrum comprises two rising peaks at 517 nm (2.40 eV) and 343 nm (3.62 eV), respectively. The lower energy peak is sharp (this can be seen more clearly from the square of

the absorbance versus photon energy curve shown in Figure 5b, although the exciton absorption does not follow the same law as band edge absorption), and it is the first exciton absorption peak of the core CsPbBr₃ NC. The PLE spectrum (emission: 550 nm) comprises also this exciton absorption peak. The higher energy peak at 3.62 eV is attributed to the exciton absorption of the CsPb₂Br₅ nanoshell, and this is consistent with the fact that CsPb₂Br₅ has a much bigger band gap compared with CsPbBr₃, as indicated by the following calculation. There are several additional even higher energy absorption peaks lying at 3.99, 4.58, and 4.84 eV, which are ascribed to the CsPb₂Br₅ nanoshell. From Figure 5a we notice a very interesting phenomenon: the rising of the UV–Vis band and decreasing of the PLE band in the range from 3.26 to 3.62 eV exhibit perfect mirror-symmetry correlation. This is because that starting from 3.26 eV the CsPb₂Br₅ nanoshell begins to absorb the incident photons more and more strongly, as a result, fewer and fewer photons can enter the inner CsPbBr₃ core, and thus the PL excitation intensity decreases in accordance. This perfect symmetric correlation between the shell-absorption increase and core-emission decrease confirms the core–shell structure of the CsPbBr₃/CsPb₂Br₅ HNCs. The PLE intensity decreases to nearly zero when the excitation photon energy exceeds 3.62 eV (Figure 5a) and this indicates that in this circumstance nearly no photons can penetrate the CsPb₂Br₅ shell to reach the CsPbBr₃ core and that there is no noticeable energy transfer from the shell to the core. This suggests that after the CsPb₂Br₅ shell absorbs higher-energy photons, the absorbed energies will be released to become thermal energies through efficient nonradiative recombination. From Figure 5b we see that the sharp exciton absorption peak of the CsPbBr₃ NCs shifts slightly to a lower energy of ~2.36 eV in the orange powder. This is because the average size of the CsPbBr₃ NC cores of the CsPbBr₃/CsPb₂Br₅ core/shell HNCs in the white powder is smaller than that of the original CsPbBr₃ NCs in the orange powder due to the phase

transition of the outer layers of the latter into the CsPb₂Br₅ nanoshell. According to the quantum confinement effect, the smaller nanoparticle has a larger energy gap, therefore, the CsPbBr₃ core NCs in the HNCs have a higher energy exciton absorption peak compared with the CsPbBr₃ NCs in the orange powder. Additionally, the CsPb₂Br₅ nanoshell forms a potential energy barrier for the electrons and holes in the CsPbBr₃ core and this slightly changes the energy gap of the latter. The influence of the potential energy barrier on the energy gap of the encapsulated semiconductor nanocrystal is because the potential energy barrier is the critical quantity in the Schrödinger equation which determines the quantum states and energy levels of the crystals.⁵⁷ Figure S7 shows the calculated band alignment of monoclinic CsPbBr₃/tetragonal CsPb₂Br₅ heterostructure by using the Fermi level equivalence law of a semiconductor heterostructure in thermal equilibrium. The calculation shows that there is an energy barrier of 0.91/1.06 eV between the conduction band minima/valence band maxima of CsPbBr₃ and CsPb₂Br₅. Although the PL spectrum of the CsPbBr₃/CsPb₂Br₅ core/shell HNCs seems to have only one maximum, however, unlike a usual emission band that follows the Gaussian function as a result of dominant inhomogeneous broadening, it cannot be fitted by using a single Gaussian function, and neither can it be fitted by a single Lorentzian function corresponding to homogeneous broadening. Instead, it can be well fitted by using a double-Gaussian function, giving rise to two band peaks centered at 524.9 nm (2.36 eV) and 526.7 nm (2.35 eV), respectively. The former sub-band has a small full width at half maximum (FWHM) of 64.3 meV, and the latter has a much bigger FWHM of 130.9 meV. This suggests that there are two radiative recombination channels in the CsPbBr₃/CsPb₂Br₅ core/shell HNCs. Because the XRD patterns (Figure 2) show no signals of other types of NCs, so the two radiative recombination channels are hardly related to different types of NCs. To verify this conjecture, we measure the time-resolved PL spectra of the orange

and white powders (Figure 5d). Both spectra can be fitted by using a biexponential function. The lifetimes (fractional intensities) of the two components for the CsPbBr₃ NCs are 8.30 μs (73.81%) and 384.3 ns (26.19%), respectively, and they decrease to 1.25 μs (78.86%) and 46.7 ns (21.14%) for the CsPbBr₃/CsPb₂Br₅ HNCs. These two decay channels indicate there are two radiative recombination channels in these HNCs which correspond to the two emission bands peaked at 524.9 and 526.7 nm. The decrease of the lifetimes of the two relaxation channels in the CsPbBr₃/CsPb₂Br₅ HNCs with respect to that in the pure CsPbBr₃ NCs may be caused by the influence of the potential barrier provided by the CsPb₂Br₅ nanoshell. The potential barrier offered by the CsPb₂Br₅ shell causes stronger spatial confinement of carriers, as a result, there could be higher degree of overlap of the wavefunctions of the electron and hole and thus the radiative quantum transition rate will be improved, this causes decrease of the lifetime. It should be noted that the reabsorption effect may also lead to two emission bands.⁵⁸

Because the optical properties are closely correlated with the electronic properties, therefore, we further calculate the electronic structures of the bulk monoclinic CsPbBr₃ and tetragonal CsPb₂Br₅ (Figure 5e,f) by using the density functional theory (DFT) calculation employing the HSE06 hybrid exchange–correlation functional. The monoclinic CsPbBr₃ has *P2* symmetry, and the original unit cell parameters employed are $a = b = 5.827 \text{ \AA}$, $c = 5.891 \text{ \AA}$ ($\alpha = \beta = 90^\circ$, $\gamma = 89.65^\circ$) (PDF#18-0364). These parameters only deviate slightly from those of cubic CsPbBr₃ and thus the electronic and optical properties of monoclinic CsPbBr₃ may resemble those of the widely studied cubic CsPbBr₃. The calculation shows that monoclinic CsPbBr₃ has a direct band gap of 2.18 eV as well as an indirect band gap of 2.09 eV (Figure 5e), whose maximum lies at the proximity of the maximum of the direct gap, and their energy difference is only 90 meV. The existence of such an indirect band gap may be related to the Rashba effect. In some perovskites

there is strong spin-orbit coupling due to the existence of the heavy elements (such as Pb and Br) which dominate the electron bands near the conduction band minimum and valence band maximum, it may result in large Rashba splitting if the crystal lacks inversion symmetry and in this circumstance the spin-degenerate parabolic band splits into two spin-polarized bands.⁵⁹⁻⁶¹ As a result, the perovskite has an indirect band gap which is slightly smaller than the direct band gap ($\Delta E \approx 50$ meV).^{59,62} The DFT calculation shows that tetragonal CsPb₂Br₅ (*I4/MCM* symmetry) is an indirect band gap semiconductor with a big band gap of 4.06 eV (Figure 5f). The indirect gap nature explains why the CsPb₂Br₅ nanoshells in the CsPbBr₃/CsPb₂Br₅ HNCs do not emit light. This agrees with the previous observation that the CsPb₂Br₅ nanosheets have no efficient luminescence.⁶³ Note that the calculated band gap of CsPb₂Br₅ is bigger than the energy of the first exciton peak (3.62 eV) and close to that of the second absorption peak (3.99 eV) (Figure 5a), and this suggests that the second absorption peak may be related to the electron transition from the valence band to the conduction band, and it also implies that CsPb₂Br₅ has a big exciton binding energy, which is characteristic of the large band gap semiconductors.^{11,12,64} As mentioned above, the DFT calculation reveals that monoclinic CsPbBr₃ has a direct band gap (2.18 eV) that is close to the indirect band gap (2.09 eV). In accordance, there may be simultaneously direct gap radiative recombination and indirect gap radiative recombination, the former is a faster decay, whereas the latter is a slow decay because the indirect-gap luminescence is an inefficient multi-order quantum process due to participation of the phonons in the electron recombination process.^{12,65} Note that although the DFT calculations were performed for bulk crystals, the currently investigated nanocrystals with sizes of a few tens of nanometers have very weak quantum confinement effect and thus the DFT calculation results can well explain their properties.

The Raman spectroscopy gives more information about the microstructures and optical properties of the CsPbBr₃ NCs and CsPbBr₃/CsPb₂Br₅ HNCs. Figure 6a shows the photos of the orange and white powders under illumination of the halogen lamp. In the photo for the orange powder, the areas in brown color are CsPbBr₃ and the small white spots are CsPb₂Br₅. Figure

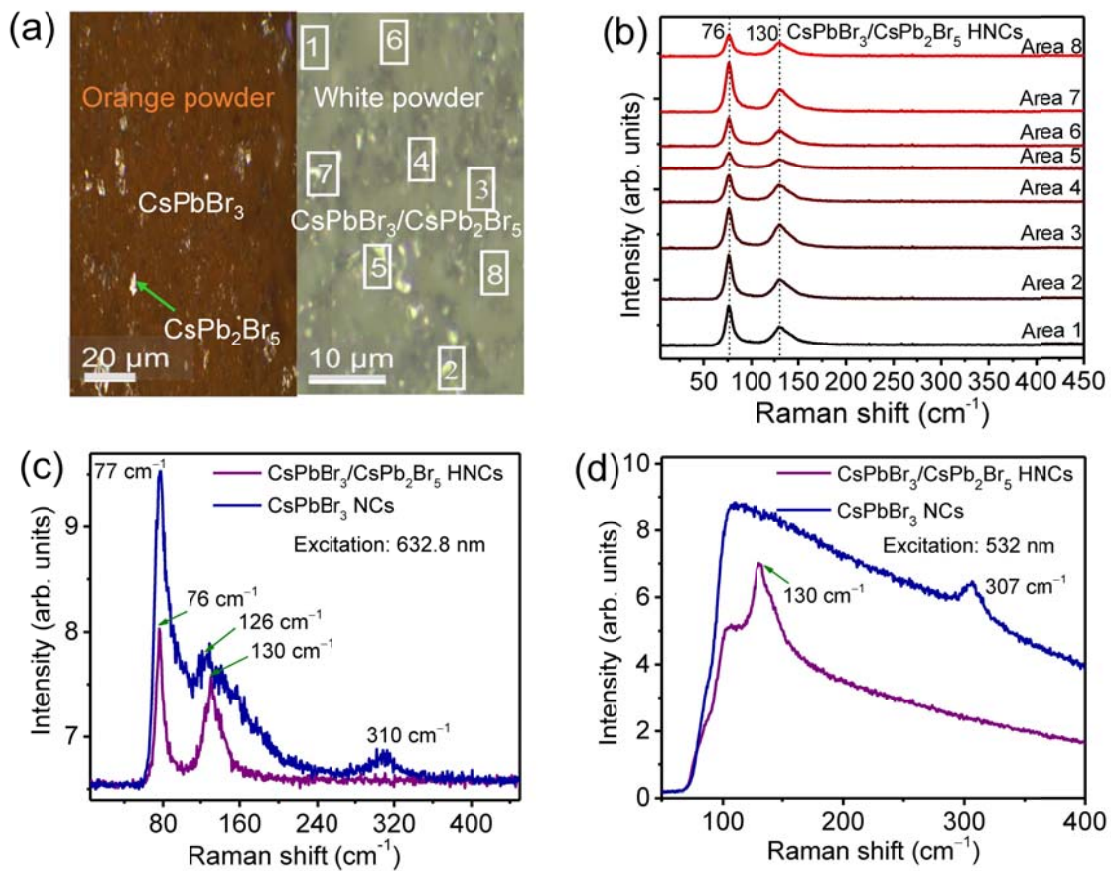


Figure 6. (a) Photographs of the CsPbBr₃ nanocrystal orange powder and the CsPbBr₃/CsPb₂Br₅ heteronanocrystal white powder under irradiation of the halogen lamp of the optical microscope. The white spots in the left part represent a small amount of CsPb₂Br₅ mixed in the orange powder. (b) Raman spectra of the CsPbBr₃/CsPb₂Br₅ heteronanocrystal white powder under 632.8-nm excitation for the eight marked regions in (a). Raman spectra of the CsPbBr₃/CsPb₂Br₅

heteronanocrystal white powder and the CsPbBr₃ nanocrystal orange powder measured under (c) 632.8-nm excitation and (d) 532-nm excitation, respectively.

6c,d show the Raman spectra of two powders measured under 632.8- and 532-nm excitation, respectively. The Raman peak at around 307–310 cm⁻¹ is characteristic of CsPbBr₃.^{51,66} It is strong in the orange powder and absent in the white powder, suggesting that all the CsPbBr₃ NCs in the white powder should be completely encapsulated by the CsPb₂Br₅ nanoshells. The wide Raman peak at around 126 cm⁻¹ in the Raman spectrum of the orange powder is also characteristic of CsPbBr₃.⁶⁷ In contrast, the Raman spectra of the white powder comprise two sharp peaks centered at 76 and 130 cm⁻¹, which are mainly contributed by CsPb₂Br₅.^{51,67} On the other hand, the energy dispersive X-ray spectroscopy (EDS) (Figure S8) of the scanning electron microscopy (SEM) indicates that the atomic ratio of Cs: Pb: Br equals 1: 1.7: 4.8 for the white powder (Table S2), which is close to the atomic ratio of the stoichiometric CsPb₂Br₅, suggesting that there are no exposed CsPbBr₃ nanoparticles in the white powder. This is confirmed by the Raman spectra measured at different areas of the white powder (Figure 6b), which exhibit no signal at 307–310 cm⁻¹ that is characteristic of CsPbBr₃. This result is expected in that the CsPbBr₃/CsPb₂Br₅ HNCs were generated in water via in situ phase transition of the original CsPbBr₃ NCs and any exposed CsPbBr₃ NCs decompose in water. The EDS (Figure S9) reveals that the atomic ratio for the orange powder is Cs: Pb: Br = 1.2: 1.0: 3.3 (Table S2), being consistent with that of stoichiometric CsPbBr₃ within the experimental error. This supports that the dominant component in the orange powder is CsPbBr₃. Note that the asymmetric broad Raman peaks (Figure 6) characteristic of CsPbBr₃ and CsPb₂Br₅ suggest there could be several

very close vibrational modes which superimpose to give rise to one seemingly asymmetric and broad peak.

We further study the thermal stability of the $\text{CsPbBr}_3/\text{CsPb}_2\text{Br}_5$ HNCs by measuring the temperature dependent PL spectra of the $\text{CsPbBr}_3/\text{CsPb}_2\text{Br}_5$ powder starting from 78 K (Figure 7a). When the temperature increases, the PL spectrum shifts to blue monotonically from 2.362 to

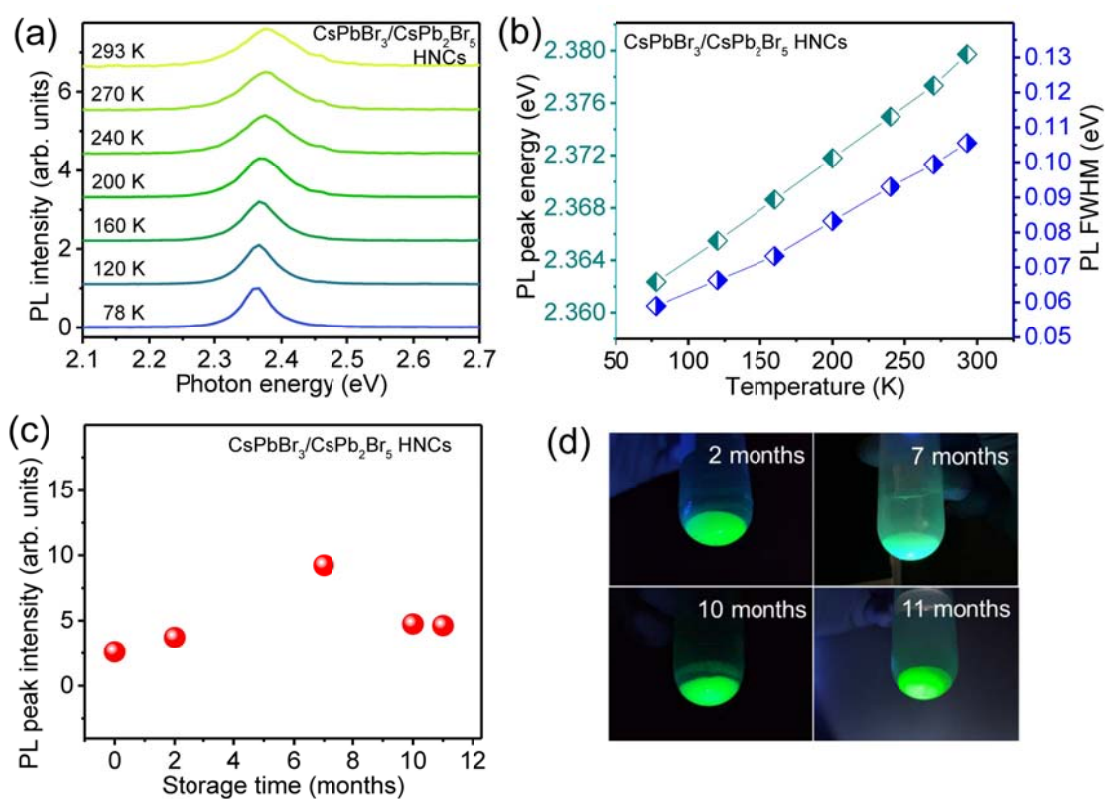


Figure 7. (a) PL spectra (excitation: 370 nm) of the $\text{CsPbBr}_3/\text{CsPb}_2\text{Br}_5$ HNC powder measured at different temperatures. (b) Plot of PL peak energy and linewidth versus temperature. (c) PL peak intensity versus storage time for the $\text{CsPbBr}_3/\text{CsPb}_2\text{Br}_5$ HNC powder immersed in water. (d) Corresponding luminescence photos taken under 365-nm excitation.

2.380 eV (Figure 7b). The absence of abrupt PL change (peak wavelength and linewidth) suggests there is no phase transition in this temperature range. The increase of energy gap with temperature is characteristic of the metal halide perovskites⁶⁴ and this is contrary to that of the conventional semiconductors.^{68–70} This abnormal temperature dependence was supposed to arise from the specific thermal expansion and electron–phonon coupling of the metal halide perovskites.⁷¹ The linewidth of the PL spectrum increases from 0.059 to 0.106 eV as the temperature increases from 78 to 293 K (Figure 7b) and this may be caused by the enhanced electron–phonon coupling at the elevated temperatures.^{64,71,72} Furthermore, the PL intensity drops gradually with increasing temperature (Figure S10) because of involvement of more phonons and enhanced nonradiative recombination.⁷³ Note that the crystal structure of the CsPbBr₃/CsPb₂Br₅ HNC powder remains unchanged during increase of temperature, as indicated by the XRD measurement (Figure S11).

As aforementioned, although the perovskites have excellent optical properties, they are usually very unstable upon exposure to heat or water. Among these unfavorable factors, water erosion to the perovskites is the most lethal. Many types of perovskites decompose rapidly in water and this causes significant decrease of the luminescence intensity. Surprisingly, we find that after the CsPbBr₃/CsPb₂Br₅ HNC powder has been immersed in water for over eleven months, its luminescence intensity remains nearly unchanged (Figure 7c,d). Figures S12 and S13 show the XRD pattern as well as PL and PLE spectra of the CsPbBr₃/CsPb₂Br₅ HNC powder after immersion in water for 11 months. Comparison with the characterizations of the pristine powder reveals both the crystal structure and the luminescence properties remain unchanged after the storage (the slight broadening of the XRD peaks for the aged sample may be caused by aggregation of some smaller nanoparticles). This proves that the CsPbBr₃/CsPb₂Br₅ HNCs have

excellent water resistance and thus the CsPb₂Br₅ nanoshells can effectively protect the green luminescent CsPbBr₃ NC cores from being eroded by water. By contrast, as shown in Figure S14, the luminescence of the pure CsPbBr₃ quantum dots suspended in toluene (see EXPERIMENTAL section for the synthesis method) vanished completely after water was added into the solution followed by shaking for 5 minutes. We further studied the thermal stability of the CsPbBr₃/CsPb₂Br₅ HNCs. The CsPbBr₃/CsPb₂Br₅ HNCs placed in a plate was heated to a specific high temperature and maintained for 0.5 h, then the PL spectrum was measured immediately right after the powder cooled down. It is found that the powder can retain 81.3% of the original luminescence intensity (at room temperature) for a test temperature of 100 °C, and for even higher test temperatures of 150 and 200 °C, the CsPbBr₃/CsPb₂Br₅ HNCs can still retain 46.7% and 19.7% of its original luminescence intensity (Figure S15). This excellent thermal stability is very impressive and suggests that the luminescent CsPbBr₃/CsPb₂Br₅ HNCs can work at high temperatures. This virtue renders them superior solid-state light emitters compared with the perovskites protected by other types of shells.⁷⁴⁻⁷⁶

2.3. Quasi-White LED Based on CsPbBr₃/CsPb₂Br₅ Core/Shell HNCs. Because the synthesized luminescent CsPbBr₃/CsPb₂Br₅ HNCs have a large yield and because they have excellent water and thermal stability, hence they may serve as the backlights in the displays. We fabricated a prototype quasi-white LED by spin coating the mixture of the CsPbBr₃/CsPb₂Br₅ HNC powder and red luminescent phosphor K₂SiF₆:Mn⁴⁺ (KSF) on the violet-emitting (380 nm) GaN chip. Figure 8b shows the electroluminescence (EL) spectrum of this LED operating at 3 V and 10 mA, and apparently it comprises three primary colors. Figure 8c displays the corresponding electroluminescence photo of the LED. It can be seen that this device emits bright quasi-white light. Figure 8a shows the Commission Internationale de L'Eclairage (CIE)

chromaticity diagram of this LED. Its color coordinates are (0.4024, 0.4647), and its color gamut is 1.2 times that of the National Television System Committee (NTSC) standard. The color

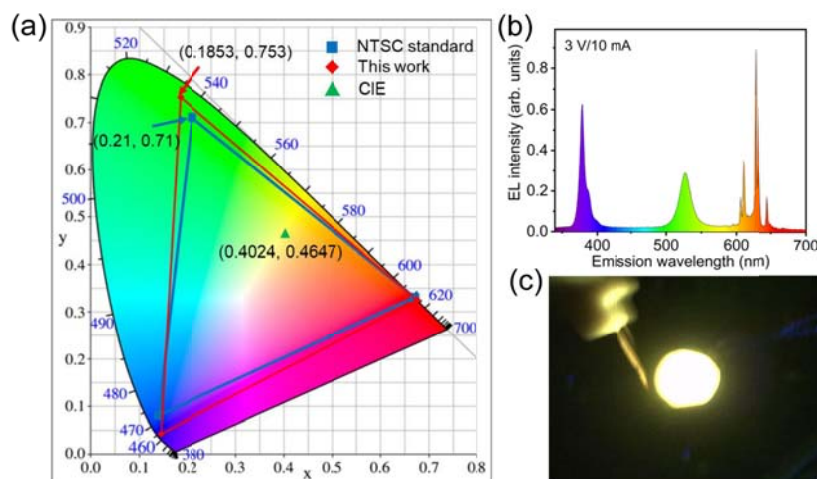


Figure 8. Characterization of a quasi-white LED constructed from a GaN chip coated by the mixture of the green luminescent CsPbBr₃/CsPb₂Br₅ HNC powder and red luminescent KSF phosphor. (a) CIE chromaticity coordinates (0.4024, 0.4647) of the LED along with its color triangle diagram and the NTSC standard triangle diagram. (b) Electroluminescence spectrum and (c) luminescence photo of this LED operating at 3 V and 10 mA.

coordinates of the green light from the CsPbBr₃/CsPb₂Br₅ HNC powder are (0.1853, 0.7530), while that of the NTSC standard green light are (0.21, 0.71) (Figure 8a and Table S3), hence the green light emitted by the CsPbBr₃/CsPb₂Br₅ HNC powder has a wider color gamut. We have also conducted the stability test of the LED device. Figure S16 shows the normalized relative intensity ratio of I_{521 nm} (CsPbBr₃/CsPb₂Br₅ HNCs): I_{380 nm} (GaN chip) versus operation time for the LED based on the core-shell HNCs. It can be seen that after 480 min of continuous operation,

the luminescence intensity of the CsPbBr₃/CsPb₂Br₅ HNC emitting layer with respect to that of the GaN chip drops to a still high value of 60.8%. This indicates that the CsPbBr₃/CsPb₂Br₅ HNCs have excellent structural and luminescence stability. These characteristics suggest they are strongly competent materials for display backlights.

3. CONCLUSIONS

In summary, we have reported the high-yield synthesis of the highly water-resistant green luminescent CsPbBr₃/CsPb₂Br₅ core/shell HNCs and deeply investigated their optical properties. The water-driven in situ self-phase transition of the original monoclinic CsPbBr₃ NCs leads to formation of the epitaxial tetragonal CsPb₂Br₅ nanoshells surrounding the luminescent CsPbBr₃ cores. The microstructural characterizations reveal that the small lattice mismatch between CsPbBr₃ and CsPb₂Br₅ accounts for the epitaxial crystallization at their interface. The optical characterizations in conjunction with the hybrid DFT calculations indicate that tetragonal CsPb₂Br₅ is an indirect wide band gap semiconductor and the CsPb₂Br₅ nanoshell forms an electron potential barrier surrounding the CsPbBr₃ core, which causes the largely enhanced double-channel exciton luminescence of the CsPbBr₃ core. These waterproof thermally-stable purely-inorganic perovskite semiconductor–semiconductor core–shell heteronanocrystals are very competent in solid-state lighting and wide color gamut displays.

4. EXPERIMENTAL AND COMPUTATIONAL DETAILS

4.1. Materials. PbBr₂ (99%, Aladdin), CsBr (99.9%, Aladdin), hydrobromic acid (HBr, 48%, Chron), and K₂SiF₆:Mn⁴⁺ (KSF, Looking Long). All chemical materials were used directly without further purification.

4.2. Synthesis of Monoclinic CsPbBr₃ Nanocrystal Powder. PbBr₂ (10 mmol) were dissolved in HBr (8 mL), and CsBr (10 mmol) was dissolved in deionized water (3 mL). Then the CsBr solution was added dropwise to the PbBr₂ solution in an ice–water bath, and the mixed solution was stirred for 1 h, during which the orange precipitate containing mainly the monoclinic CsPbBr₃ NCs was produced rapidly. The precipitate was filtered and washed three times with ethanol and then dried in a vacuum drying oven at 60 °C in the dark for 12 h.

4.3. Synthesis of CsPbBr₃/CsPb₂Br₅ Heteronanocrystal Powder. The deionized water was added into the as-prepared CsPbBr₃ NC powder, during which the color of the powder changed gradually from orange to white. After stirring for 1.5 h, the powder turned into white completely, which was collected by using the suction filtration. Subsequently, it was dried in a vacuum drying oven at 60 °C in the dark for 12 h.

4.4. Synthesis of CsPbBr₃ quantum dots. The CsPbBr₃ quantum dots with a most probable size of 6.8 nm were synthesized by using the conventional method.⁴ PbBr₂ (0.069 g) and 1-octadecene (ODE) (5 mL) were added into a three-necked flask and then dried at 120 °C for 2 h under an argon atmosphere. Then, the dry oleylamine (OLA) (0.5 mL) and oleic acid (OA) (0.5 mL) were injected into the flask at 120 °C under an argon atmosphere. After the PbBr₂ salt was completely dissolved, the reaction temperature was improved to 140 °C, and then Cs-oleate solution (0.4 mL) was quickly injected into the three-necked flask. After 5 s, the reaction solution was cooled to room temperature in an ice–water bath. After addition of tert-butanol (tBuOH, ODE:tBuOH = 1:1 in volume ratio), the crude solution was centrifuged to generate precipitated CsPbBr₃ quantum dots, which were then dissolved in toluene.

4.5. Fabrication of the Quasi-White LED. 0.36 g CsPbBr₃/CsPb₂Br₅ powder and 0.18 g red luminescent phosphor K₂SiF₆:Mn⁴⁺ (KSF) powder were introduced into 1.217 g organic silica

gel, and the mixture was stirred evenly with a glass rod. The mixed glue was uniformly coated onto a GaN chip (emission: 380 nm). It was then put in a blast drying box and annealed at 100 °C for 1 h.

4.6. Characterization. The Fluorlog3-TCSPC spectrofluorometer (HORIBA JOBIN YVON) equipped the Xe lamp (excitation wavelengths employed: 360–500 nm) and pulsed laser diodes was used to measure the PL, PL excitation, and time-resolved PL spectra at room temperature. The quantum yield was acquired by using the integration sphere under excitation of a Xe lamp. The low temperature PL spectra were measured under 370-nm excitation by cooling the samples with liquid nitrogen. The TEM characterization was performed on a Tecnai G2 T20 TEM (FEI) operating at 200 kV. The Smartlab (3) intelligent X-ray diffractometer was used for the X-ray diffraction characterization. The UV–Vis absorption spectra were measured by using a UV–Vis spectrophotometer (HITACHI UV-3600Plus). The LabRAM HR 800 Raman spectrometer (HORIBA JOBIN YVON) and Witec Alpha300RA Raman spectrometer were used to conduct the Raman spectroscopy under 532-nm and 632.87-nm laser excitation. The scanning electron microscope (FEI Inspect F50) equipped with an energy dispersive X-ray spectrometer (EDS) probe was used for the SEM observation and elemental analysis. The Acton SP-2358 Spectrometer (Princeton Instruments) was used to measure the electroluminescence spectra. The bias was applied on the LED by using a Keithley 2400 source meter in air at room temperature.

4.7. Computation Methods. The density functional theory calculations were implemented in the Vienna ab initio simulation package (VASP) code.⁷⁷ The interaction between the ions and electrons was described by using the projector augmented wave (PAW) method.⁷⁸ The Perdew–Burke–Ernzerhof (PBE) exchange–correlation functional⁷⁹ within the generalized gradient approximation (GGA) was employed for the geometric optimization with a force tolerance for

ionic relaxation of 0.3 eV/Å. The HSE06 hybrid functional^{80,81} was used for the calculation of the electronic structure. The cut-off energy of 300 eV (accurate enough, as can be seen from the convergence test shown in Figure S17) was used for the plane-wave expansions in all the calculations. The calculations were performed using a 4×4×4 Gamma centered grid. The band alignment of monoclinic CsPbBr₃/tetragonal CsPb₂Br₅ heterostructure (Figure S7) was calculated by using the Fermi level equivalence law of a semiconductor heterostructure in thermal equilibrium.⁸⁰ The Fermi level of an intrinsic semiconductor follows:⁸²

$$E_{Fi} = E_v + \frac{1}{2}E_g - \frac{1}{2}k_B T \ln\left(\frac{N_c}{N_v}\right), \quad (1)$$

where k_B is the Boltzmann constant, T (300 K) is the absolute temperature, E_v and E_g are the valence band maximum energy level and bandgap, and the effective density of states at the conduction/valence band edge is given by:

$$N_c = 2[2\pi m_e^* k_B T / h^2]^{3/2} \quad (2)$$

$$N_v = 2[2\pi m_h^* k_B T / h^2]^{3/2} \quad (3)$$

In these equations, m_e^* and m_h^* are the effective mass of electron at the conduction band minimum and that of hole at the valence band maximum, h is the Planck constant. The effective mass-tensor was calculated by using the effective mass calculator (EMC) code⁸³ that is based on the VASP calculation results. The calculated bandgaps, effective masses, and Fermi level shift relative to the middle point of the forbidden gap are listed in Table S1.

ACKNOWLEDGMENT

This work was supported by the National Natural Science Foundation of China No. 11874106.

REFERENCES

- (1) Akkerman, Q. A.; Rainò, G.; Kovalenko, M. V.; Manna, L. Genesis, Challenges and Opportunities for Colloidal Lead Halide Perovskite Nanocrystals. *Nat. Mater.* **2018**, *17*, 394–405.
- (2) Yang B.; Han, K. Charge-Carrier Dynamics of Lead-Free Halide Perovskite Nanocrystals. *Acc. Chem. Res.* **2019**, *52*, 3188–3198.
- (3) Green, M. A.; Dunlop, E. D.; Hohl-Ebinger, J.; Yoshita, M.; Kopidakis, N.; Hao, X.; Solar Cell Efficiency Tables (Version 56). *Prog. Photovoltaics* **2020**, *28*, 629–638.
- (4) Wu, W.; Zhang, Y.; Liang, T.; Fan, J.; Carrier Accumulation Enhanced Auger Recombination and Inner Self-Heating-Induced Spectrum Fluctuation in CsPbBr₃ Perovskite Nanocrystal Light-Emitting Devices. *Appl. Phys. Lett.* **2019**, *115*, 243503.
- (5) Lin, K.; Xing, J.; Quan, L. N.; de Arquer, F. P. G.; Gong, X.; Lu, J.; Xie, L.; Zhao, W.; Zhang, D.; Yan, C.; Li, W.; Liu, X.; Lu, Y.; Kirman, J.; Sargent, E. H.; Xiong, Q.; Wei, Z. Perovskite Light-Emitting Diodes with External Quantum Efficiency Exceeding 20 per cent. *Nature* **2018**, *562*, 245–248.
- (6) Cao, Y.; Wang, N.; Tian, H.; Guo, J.; Wei, Y.; Chen, H.; Miao, Y.; Zou, W.; Pan, K.; He, Y.; Cao, H.; Ke, Y.; Xu, M.; Wang, Y.; Yang, M.; Du, K.; Fu, Z.; Kong, D.; Dai, D.; Jin, Y.; Li, G.; Li, H.; Peng, Q.; Wang, J.; Huang, W. Perovskite Light-Emitting Diodes Based on Spontaneously Formed Submicrometre-Scale Structures. *Nature* **2018**, *562*, 249–253.
- (7) Fang, Z.; Chen, W.; Shi, Y.; Zhao, J.; Chu, S.; Zhang, J.; Xiao, Z. Dual Passivation of Perovskite Defects for Light-Emitting Diodes with External Quantum Efficiency Exceeding 20%. *Adv. Funct. Mater.* **2020**, *30*, 1909754 .
- (8) Smith, M. D.; Connor, B. A.; Karunadasa, H. I. Tuning the Luminescence of Layered Halide Perovskites. *Chem. Rev.* **2019**, *119*, 3104–3139.

- (9) Akkerman, Q. A.; Abdelhady, A. L.; Manna, L. Zero-Dimensional Cesium Lead Halides: History, Properties, and Challenges. *J. Phys. Chem. Lett.* **2018**, *9*, 2326–2337.
- (10) Smith, M. D.; Karunadasa, H. I. White-Light Emission from Layered Halide Perovskites. *Acc. Chem. Res.* **2018**, *51*, 619–627.
- (11) Zhang, Y.; Fan, B.; Liu, Y.; Li, H.; Deng, K.; Fan, J. Quasi-Self-Trapped Frenkel-Exciton Near-UV Luminescence with Large Stokes Shift in Wide-Bandgap Cs₄PbCl₆ Nanocrystals. *Appl. Phys. Lett.* **2018**, *112*, 183101.
- (12) Zhang, Y.; Li, Y.; Liu, Y.; Li, H.; Fan, J. Quantum Confinement Luminescence of Trigonal Cesium Lead Bromide Quantum Dots. *Appl. Surf. Sci.* **2019**, *466*, 119–125.
- (13) Niu, G.; Li, W.; Meng, F.; Wang, L.; Dong, H.; Qiu, Y. Study on the stability of CH₃NH₃PbI₃ films and the effect of post-modification by aluminum oxide in all-solid-state hybrid solar cells. *J. Mater. Chem. A* **2014**, *2*, 705.
- (14) Berry, J.; Buonassisi, T.; Egger, D. A.; Hodes, G.; Kronik, L.; Loo, Y. L.; Lubomirsky, I.; Marder, S. R.; Mastai, Y.; Miller, J. S.; Mitzi, D. B.; Paz, Y.; Rappe, A. M.; Riess, I.; Rybtchinski, B.; Stafsudd, O.; Stevanovic, V.; Toney, M. F.; Zitoun, D.; Kahn, A.; Ginley, D.; Cahen, D. Hybrid Organic–Inorganic Perovskites (HOIPs): Opportunities and Challenges. *Adv. Mater.* **2015**, *27*, 5102–5112.
- (15) Leijtens, T.; Eperon, G. E.; Noel, N. K.; Habisreutinger, S. N.; Petrozza, A.; Snaith, H. J. Stability of Metal Halide Perovskite Solar Cells. *Adv. Energy Mater.* **2015**, *5*, 1500963.
- (16) Wang, W.; Zhang, Y.; Wu, W.; Liu, X.; Ma, X.; Qian, G.; Fan, J. Quantitative Modeling of Self-Assembly Growth of Luminescent Colloidal CH₃NH₃PbBr₃ Nanocrystals. *J. Phys. Chem. C* **2019**, *123*, 13110–13121.
- (17) Niu, G.; Guo, X.; Wang, L. Review of Recent Progress in Chemical Stability of Perovskite

Solar Cells. *J. Mater. Chem. A* **2015**, *3*, 8970.

(18) Rong, Y.; Liu, L.; Mei, A.; Li, X.; Han, H. Beyond Efficiency: the Challenge of Stability in Mesoscopic Perovskite Solar Cells. *Adv. Energy Mater.* **2015**, *5*, 1501066.

(19) Chen, S.; Zhang, X.; Zhao, J.; Zhang, Y.; Kong, G.; Li, Q.; Li, N.; Yu, Y.; Xu, N.; Zhang, J.; Liu, K.; Zhao, Q.; Cao, J.; Feng, J.; Li, X.; Qi, J.; Yu, D.; Li, J.; Gao, P. Atomic Scale Insights into Structure Instability and Decomposition Pathway of Methylammonium Lead Iodide Perovskite. *Nat. Commun.* **2018**, *9*, 4807.

(20) Wells, H. L.; Johnston, W. R. Über die Ammoniumbleihalogenide. *Z. Anorg. Chem.* **1893**, *3*, 195.

(21) Li, X.; Wu, Y.; Zhang, S.; Cai, B.; Gu, Y.; Song, J.; Zeng, H. CsPbX₃ Quantum Dots for Lighting and Displays: Room-Temperature Synthesis, Photoluminescence Superiorities, Underlying Origins and White Light-Emitting Diodes. *Adv. Funct. Mater.* **2016**, *26*, 2435–2445.

(22) Nedelcu, G.; Protesescu, L.; Yakunin, S.; Bodnarchuk, M. I.; Grotevent, M. J.; Kovalenko, M. V. Fast Anion-Exchange in Highly Luminescent Nanocrystals of Cesium Lead Halide Perovskites (CsPbX₃, X = Cl, Br, I). *Nano Lett.* **2015**, *15*, 5635–5640.

(23) Protesescu, L.; Yakunin, S.; Bodnarchuk, M. I.; Krieg, F.; Caputo, R.; Hendon, C. H.; Yang, R. X.; Walsh, A.; Kovalenko, M. V. Nanocrystals of Cesium Lead Halide Perovskites (CsPbX₃, X = Cl, Br, and I): Novel Optoelectronic Materials Showing Bright Emission with Wide Color Gamut. *Nano Lett.* **2015**, *15*, 3692–3696.

(24) Song, J.; Li, J.; Li, X.; Xu, L.; Dong, Y.; Zeng, H. Quantum Dot Light-Emitting Diodes Based on Inorganic Perovskite Cesium Lead Halides (CsPbX₃). *Adv. Mater.* **2015**, *27*, 7162–7167.

(25) An, R.; Zhang, F.; Zou, X.; Tang, Y.; Liang, M.; Oshchapovskyy, I.; Liu, Y.; Honarfar, A.;

Zhong, Y.; Li, C.; Geng, H.; Chen, J.; Canton, S. E.; Pullerits, T.; Zheng, K. Photostability and Photodegradation Processes in Colloidal CsPbI₃ Perovskite Quantum Dots. *ACS Appl. Mater. Interfaces* **2018**, *10*, 39222–39227.

(26) Huang, S.; Li, Z.; Wang, B.; Zhu, N.; Zhang, C.; Kong, L.; Zhang, Q.; Shan, A.; Li, L. Morphology Evolution and Degradation of CsPbBr₃ Nanocrystals under Blue Light-Emitting Diode Illumination. *ACS Appl. Mater. Interfaces* **2017**, *9*, 7249–7258.

(27) Yuan, X.; Hou, X.; Li, J.; Qu, C.; Zhang, W.; Zhao, J.; Li, H. Thermal Degradation of Luminescence in Inorganic Perovskite CsPbBr₃ Nanocrystals. *Phys. Chem. Chem. Phys.* **2017**, *19*, 8934.

(28) Chen, J.; Liu, D.; Al-Marri, M. J.; Nuuttila, L.; Lehtivuori, H.; Zheng, K. Photo-Stability of CsPbBr₃ Perovskite Quantum Dots for Optoelectronic Application. *Sci. China Mater.* **2016**, *59*, 719–727.

(29) Battaglia, D.; Li, J. J.; Wang, Y.; Peng, X. Colloidal Two-Dimensional Systems: CdSe Quantum Shells and Wells. *Angew. Chem. Int. Ed.* **2003**, *42*, 5035–5039.

(30) Donega, C. D. Formation of Nanoscale Spatially Indirect Excitons: Evolution of the Type-II Optical Character of CdTe/CdSe Heteronanocrystals. *Phys. Rev. B* **2010**, *81*, 165303.

(31) Hines, M. A.; Guyot-Sionnest, P. Synthesis and Characterization of Strongly Luminescing ZnS-Capped CdSe Nanocrystals. *J. Phys. Chem.* **1996**, *100*, 468–471.

(32) Ivanov, S. A.; Piryatinski, A.; Nanda, J.; Tretiak, S.; Zavadil, K. R.; Wallace, W. O.; Werder, D.; Klimov, V. I. Type-II Core/Shell CdS/ZnSe Nanocrystals: Synthesis, Electronic Structures, and Spectroscopic Properties. *J. Am. Chem. Soc.* **2007**, *129*, 11708–11719.

(33) Kim, S.; Fisher, B.; Eisler, H. J.; Bawendi, M. Type-II Quantum Dots: CdTe/CdSe(Core/Shell) and CdSe/ZnTe(Core/Shell) Heterostructures. *J. Am. Chem. Soc.* **2003**,

125, 11466–11467.

(34) Zhong, X.; Xie, R.; Zhang, Y.; Basché, T.; Knoll, W. High-Quality Violet- to Red-Emitting ZnSe/CdSe Core/Shell Nanocrystals. *Chem. Mater.* **2005**, *17*, 4038–4042.

(35) Reiss, P.; Protiere, M.; Li, L. Core/Shell Semiconductor Nanocrystals. *Small* **2009**, *5*, 154–168.

(36) Chen, J. S.; Yang, B.; Li, C. S.; Zheng, K. B.; Zidek, K.; Pullerits, T. Photostability of the Oleic Acid-Encapsulated Water-Soluble $\text{Cd}_x\text{Se}_y\text{Zn}_{1-x}\text{S}_{1-y}$ Gradient Core-Shell Quantum Dots. *ACS Omega* **2017**, *2*, 1922–1929.

(37) Bera, S.; Pradhan, N. Perovskite Nanocrystal Heterostructures: Synthesis, Optical Properties, and Applications. *ACS Energy Lett.* **2020**, *5*, 2858–2872.

(38) Zhong, Q.; Cao, M.; Hu, H.; Yang, D.; Chen, M.; Li, P.; Wu, L.; Zhang, Q. One-Pot Synthesis of Highly Stable $\text{CsPbBr}_3@\text{SiO}_2$ Core-Shell Nanoparticles. *ACS Nano* **2018**, *12*, 8579–8587.

(39) Li, Z.-J.; Hofman, E.; Li, J.; Davis, A. H.; Tung, C.-H.; Wu, L.-Z.; Zheng, W. Photoelectrochemically Active and Environmentally Stable $\text{CsPbBr}_3/\text{TiO}_2$ Core/Shell Nanocrystals. *Adv. Funct. Mater.* **2018**, *28*, 1704288.

(40) Chen, D.; Fang, G.; Chen, X. Silica-Coated Mn-Doped $\text{CsPb}(\text{Cl}/\text{Br})_3$ Inorganic Perovskite Quantum Dots: Exciton-to-Mn Energy Transfer and Blue-Excitable Solid-State Lighting. *ACS Appl. Mater. Interfaces* **2017**, *9*, 40477–40487.

(41) Liu, H.; Tan, Y.; Cao, M.; Hu, H.; Wu, L.; Yu, X.; Wang, L.; Sun, B.; Zhang, Q. Fabricating CsPbX_3 -Based Type I and Type II Heterostructures by Tuning the Halide Composition of Janus $\text{CsPbX}_3/\text{ZrO}_2$ Nanocrystals. *ACS Nano* **2019**, *13*, 5366–5374.

(42) Wang, B.; Zhang, S.; Liu, B.; Li, J.; Cao, B.; Liu, Z. Stable $\text{CsPbBr}_3:\text{Sn}@\text{SiO}_2$ and

Cs₄PbBr₆:Sn@SiO₂ Core–Shell Quantum Dots with Tunable Color Emission for Light-Emitting Diodes. *ACS Appl. Nano Mater.* **2020**, *3*, 3019–3027.

(43) Xu, L.; Chen, J.; Song, J.; Li, J.; Xue, J.; Dong, Y.; Cai, B.; Shan, Q.; Han, B.; Zeng, H. Double-Protected All-Inorganic Perovskite Nanocrystals by Crystalline Matrix and Silica for Triple-Modal Anti-Counterfeiting Codes. *ACS Appl. Mater. Interfaces* **2017**, *9*, 26556–26564.

(44) Fan, C.; Xu, X.; Yang, K.; Jiang, F.; Wang, S.; Zhang, Q. Controllable Epitaxial Growth of Core–Shell PbSe@CsPbBr₃ Wire Heterostructures. *Adv. Mater.* **2018**, *30*, 1804707.

(45) Zhang, X.; Lu, M.; Zhang, Y.; Wu, H.; Shen, X.; Zhang, W.; Zheng, W.; Colvin, V. L.; Yu, W. W. PbS Capped CsPbI₃ Nanocrystals for Efficient and Stable Light-Emitting Devices Using p–i–n Structures. *ACS Cent. Sci.* **2018**, *4*, 1352–1359.

(46) Ravi, V. K.; Saikia, S.; Yadav, S.; Nawale, V. V.; Nag, A. CsPbBr₃/ZnS Core/Shell Type Nanocrystals for Enhancing Luminescence Lifetime and Water Stability. *ACS Energy Lett.* **2020**, *5*, 1794–1796.

(47) Tang, X.; Yang, J.; Li, S.; Liu, Z.; Hu, Z.; Hao, J.; Du, J.; Leng, Y.; Qin, H.; Lin, X.; Lin, Y.; Tian, Y.; Zhou, M.; Xiong, Q. Single Halide Perovskite/Semiconductor Core/Shell Quantum Dots with Ultrastability and Nonblinking Properties. *Adv. Sci.* **2019**, *6*, 1900412.

(48) Rodová, M.; Brožek, J.; Knížek, K.; Nitsch, K. Phase Transitions in Ternary Caesium Lead Bromide. *J. Ther. Anal. Calorim.* **2003**, *71*, 667–673.

(49) Huang, Z. P.; Ma, B.; Wang, H.; Li, N.; Liu, R. T.; Zhang, Z. Q.; Zhang, X. D.; Zhao, J. H.; Zheng, P. Z.; Wang, Q.; Zhang, H. L. In Situ Growth of 3D/2D (CsPbBr₃/CsPb₂Br₅) Perovskite Heterojunctions toward Optoelectronic Devices. *J. Phys. Chem. Lett.* **2020**, *11*, 6007–6015.

(50) Li, J.; Zhang, H.; Wang, S.; Long, D.; Li, M.; Guo, Y.; Zhong, Z.; Wu, K.; Wang, D.;

Zhang, T. Synthesis of All-Inorganic CsPb₂Br₅ Perovskite and Determination of its Luminescence Mechanism. *RSC Adv.* **2017**, *7*, 54002.

(51) Wang, C.; Wang, Y.; Su, X.; Hadjiev, V. G.; Dai, S.; Qin, Z.; Calderon Benavides, H. A.; Ni, Y.; Li, Q.; Jian, J.; Alam, M. K.; Wang, H.; Robles Hernandez, F. C.; Yao, Y.; Chen, S.; Yu, Q.; Feng, G.; Wang, Z.; Bao, J. Extrinsic Green Photoluminescence from the Edges of 2D Cesium Lead Halides. *Adv. Mater.* **2019**, *31*, 1902492.

(52) Tong, G.; Li, H.; Li, D.; Zhu, Z.; Xu, E.; Li, G.; Yu, L.; Xu, J.; Jiang, Y. Dual-Phase CsPbBr₃-CsPb₂Br₅ Perovskite Thin Films via Vapor Deposition for High-Performance Rigid and Flexible Photodetectors. *Small* **2018**, *14*, 1702523.

(53) Zheng, Y.; Yang, T.; Fang, Z.; Shang, M.; Zhang, Z.; Yang, J.; Fan, J.; Yang, W.; Hou, X.; Wu, T. All-Inorganic Dual-Phase Halide Perovskite Nanorings. *Nano Res.* **2020**, *13*, 2994–3000.

(54) Turedi, B.; Lee, K. J.; Dursun, I.; Alamer, B.; Wu, Z.; Alarousu, E.; Mohammed, O. F.; Cho, N.; Bakr, O. M. Water-Induced Dimensionality Reduction in Metal-Halide Perovskites. *J. Phys. Chem. C* **2018**, *122*, 14128–14134.

(55) Reiss, P.; Protière, M.; Li, L. Core/Shell Semiconductor Nanocrystals. *Small* **2009**, *5*, 154–168.

(56) Fan, J. Y.; Wu, X. L.; Li, H. X.; Liu, H. W.; Siu, G. G.; Chu, P. K. Luminescence from Colloidal 3C-SiC Nanocrystals in Different Solvents. *Appl. Phys. Lett.* **2006**, *88*, 041909.

(57) Pellegrini, G.; Mattei, G.; Mazzoldi, P. Finite Depth Square Well Model: Applicability and Limitations. *J. Appl. Phys.* **2005**, *97*, 073706.

(58) Yang, B.; Zhang, F.; Chen, J.; Yang, S.; Xia, X.; Pullerits, T.; Deng, W.; Han, K. Ultrasensitive and Fast All-Inorganic Perovskite-Based Photodetector via Fast Carrier Diffusion. *Adv. Mater.* **2017**, *29*, 1703758–1703766.

- (59) Martiradonna, L. Riddles in Perovskite Research. *Nat. Mater.* **2018**, *17*, 377–384.
- (60) Yin, J.; Maity, P.; Xu, L.; El-Zohry, A. M.; Li, H.; Bakr, O. M.; Brédas, J.-L.; Mohammed, O. F. Layer-Dependent Rashba Band Splitting in 2D Hybrid Perovskites. *Chem. Mater.* **2018**, *30*, 8538–8545.
- (61) Yaffe, O.; Guo, Y.; Tan, L. Z.; Egger, D. A.; Hull, T.; Stoumpos, C. C.; Zheng, F.; Heinz, T. F.; Kronik, L.; Kanatzidis, M. G.; Owen, J. S.; Rappe, A. M.; Pimenta, M. A.; Brus, L. E. Local Polar Fluctuations in Lead Halide Perovskite Crystals. *Phys. Rev. Lett.* **2017**, *118*, 136001.
- (62) Hutter, E. M.; Gelvez-Rueda, M. C.; Osherov, A.; Bulovic, V.; Grozema, F. C.; Stranks, S. D.; Savenije, T. J. Direct–indirect character of the bandgap in methylammonium lead iodide perovskite. *Nat. Mater.* **2017**, *16*, 115–120.
- (63) Li, G.; Wang, H.; Zhu, Z.; Chang, Y.; Zhang, T.; Song, Z.; Jiang, Y. Shape and phase evolution from CsPbBr₃ perovskite nanocubes to tetragonal CsPb₂Br₅ nanosheets with an indirect bandgap. *Chem. Commun.* **2016**, *52*, 11296.
- (64) Liu, X.; Wu, W.; Zhang, Y.; Li, Y.; Wu, H.; Fan, J.; Critical Roles of High- and Low-Frequency Optical Phonons in Photodynamics of Zero-Dimensional Perovskite-like (C₆H₂₂N₄Cl₃)SnCl₃ Crystals. *J. Phys. Chem. Lett.* **2019**, *10*, 7586–7593.
- (65) Zhang, X.; Shen, J. X.; Van de Walle, C. G. Three-Dimensional Spin Texture in Hybrid Perovskites and Its Impact on Optical Transitions. *J. Phys. Chem. Lett.* **2018**, *9*, 2903–2908.
- (66) Cha, J. H.; Han, J. H.; Yin, W.; Park, C.; Park, Y.; Ahn, T. K.; Cho, J. H.; Jung, D. Y. *J. Phys. Chem. Lett.* **2017**, *8*, 565.
- (67) Liu, M.; Zhao, J.; Luo, Z.; Sun, Z.; Pan, N.; Ding, H.; Wang, X. Unveiling Solvent-Related Effect on Phase Transformations in CsBr–PbBr₂ System: Coordination and Ratio of Precursors. *Chem. Mater.* **2018**, *30*, 5846–5852.

- (68) Chon, B.; Bang, J.; Park, J.; Jeong, C.; Choi, J. H.; Lee, J.-B.; Joo, T.; Kim, S. Unique Temperature Dependence and Blinking Behavior of CdTe/CdSe (Core/Shell) Type-II Quantum Dots. *J. Phys. Chem. C* **2010**, *115*, 436–442.
- (69) Valerini, D.; Cretí, A.; Lomascolo, M.; Manna, L.; Cingolani, R.; Anni, M. Temperature Dependence of the Photoluminescence Properties of Colloidal CdSe/ZnS Core/Shell Quantum Dots Embedded in a Polystyrene Matrix. *Phys. Rev. B* **2005**, *71*, 235409.
- (70) O'Donnell, K. P.; Chen, X. Temperature Dependence of Semiconductor Band Gaps. *Appl. Phys. Lett.* **1991**, *58*, 2924.
- (71) Rudin, S.; Reinecke, T. L.; Segall, B. Temperature-Dependent Exciton Linewidths in Semiconductors. *Phys. Rev. B* **1990**, *42*, 11218–11231.
- (72) Wright, A. D.; Verdi, C.; Milot, R. L.; Eperon, G. E.; Perez-Osorio, M. A.; Snaith, H. J.; Giustino, F.; Johnston, M. B.; Herz, L. M. Electron–Phonon Coupling in Hybrid Lead Halide Perovskites. *Nat. Commun.* **2016**, *7*, 11755.
- (73) Diroll, B. T.; Nedelcu, G.; Kovalenko, M. V.; Schaller, R. D. High-Temperature Photoluminescence of CsPbX₃ (X = Cl, Br, I) Nanocrystals. *Adv. Funct. Mater.* **2017**, *27*, 1606750.
- (74) Hu, H.; Wu, L.; Tan, Y.; Zhong, Q.; Chen, M.; Qiu, Y.; Yang, D.; Sun, B.; Zhang, Q.; Yin, Y. Interfacial Synthesis of Highly Stable CsPbX₃/Oxide Janus Nanoparticles. *J. Am. Chem. Soc.* **2018**, *140*, 406–412.
- (75) Li, L.; Zhang, Z.; Chen, Y.; Xu, Q.; Zhang, J. R.; Chen, Z.; Chen, Y.; Zhu, J. J. Sustainable and Self-Enhanced Electrochemiluminescent Ternary Suprastructures Derived from CsPbBr₃ Perovskite Quantum Dots. *Adv. Funct. Mater.* **2019**, *29*, 1902533.
- (76) Liang, X.; Chen, M.; Wang, Q.; Guo, S.; Yang, H. Ethanol-Precipitable, Silica-Passivated

Perovskite Nanocrystals Incorporated into Polystyrene Microspheres for Long-Term Storage and Reusage. *Angew. Chem. Int. Ed.* **2019**, *58*, 2799.

(77) Kresse, G.; Furthmüller, J. Efficient Iterative Schemes for ab initio Total-Energy Calculations Using a Plane-Wave Basis Set. *Phys. Rev. B* **1996**, *54*, 11169.

(78) Kresse, G.; Joubert, D. P. From Ultrasoft Pseudopotentials to the Projector Augmented-Wave Method. *Phys. Rev. B* **1999**, *59*, 1758.

(79) Perdew, J. P.; Burke, K.; Ernzerhof, M. Generalized Gradient Approximation Made Simple. *Phys. Rev. Lett.* **1996**, *77*, 3865–3868.

(80) Heyd, J.; Scuseria, G. E.; Ernzerhof, M. Hybrid Functionals Based on a Screened Coulomb Potential. *J. Chem. Phys.* **2003**, *118*, 8207–8215.

(81) Krukau, A. V.; Vydrov, O. A.; Izmaylov, A. F.; Scuseria, G. E. Hybrid Functionals Based on a Screened Coulomb Potential. *J. Chem. Phys.* **2006**, *125*, 224106.

(82) Kasap, S. O. *Optoelectronics and Photonics: Principles and Practices*, 2nd ed.; Pearson Education, Inc.: Upper Saddle River, 2013,

(83) Fonari, A.; Sutton, C. *Effective Mass Calculator*, 2012.